applied sciences

MDPI

Article

Analysis of Altitude and Ambient Temperature Effects on the Reactivity of Oxidation Catalysts in the Presence of H_2

José Ramón Serrano, Pedro Piqueras *, Enrique José Sanchis and Carla Conde

CMT-Clean Mobility & Thermofluids, Universitat Politècnica de València, Camino de Vera s/n, 46022 Valencia, Spain; jrserran@upv.edu.es (J.R.S.); ensanpac@upv.edu.es (E.J.S.); cconcor@upv.edu.es (C.C.)
* Correspondence: pedpicab@upv.edu.es; Tel.: +34-963877650

Abstract: Worldwide emission standards are now required to cover engine operation under extreme ambient conditions, which affect the raw emissions and the efficiency of the exhaust aftertreatment systems. These regulations also target new combustion technologies for decarbonization, such as neat hydrogen (H_2) combustion or dual-fuel strategies, which involve a challenge to the analysis of exhaust aftertreatment system requirements and performance. This work addresses the impact of high altitude and low ambient temperature conditions on the reactivity of an oxidation catalyst in the presence of H_2. A reaction mechanism is proposed to cover the main conversion paths of CO, HC, and H_2, including the formation and consumption of high-energy surface reaction intermediates. The mechanism has been implemented into a faster-than-real-time reduced-order model for multi-layer washcoat honeycomb catalytic converters. The model was utilized to investigate the effect of H_2 concentration on the reactivity of CO and HC within the catalyst under various operating and ambient conditions. By applying the model and examining the selectivity towards different reaction pathways in the presence of H_2, insights into surface intermediates and reactivity across different cross-sections of the monolith were obtained. This analysis discusses the underlying causes of reactivity changes promoted by H_2 and its relative importance as a function of driving boundary conditions.

Keywords: hydrogen; emissions; altitude; exhaust aftertreatment system; ambient temperature; low temperature; light-off

Citation: Serrano, J.R.; Piqueras, P.; Sanchis, E.J.; Conde, C. Analysis of Altitude and Ambient Temperature Effects on the Reactivity of Oxidation Catalysts in the Presence of H_2. *Appl. Sci.* **2024**, *14*, 4790. https://doi.org/10.3390/app14114790

Academic Editor: Leonarda Liotta

Received: 30 April 2024
Revised: 29 May 2024
Accepted: 29 May 2024
Published: 31 May 2024

1. Introduction

Stringent emissions regulations reflect growing societal demands for cleaner and more sustainable transportation [1]. The introduction of Real Driving Emissions (RDE) testing and the Worldwide Harmonized Light Duty Test Cycle (WLTC) within the Worldwide Harmonized Light Vehicles Test Procedure (WLTP) framework aims to narrow the gap between homologation and real-world emissions of internal combustion engines (ICEs) [2]. However, research indicates that vehicles meeting current standards still emit significant pollutants under specific conditions, such as cold starts [3], short trips [4], and scenarios involving high altitudes [5] or extreme ambient temperatures [6]. Current RDE tests establish environmental limits to assess vehicle emissions control in real-world driving scenarios [7]. These tests define two categories: moderate conditions (altitude 0–700 m, temperature 0–30 °C) and extended conditions (altitude 700–1300 m, temperature −7 to 35 °C) [8]. Furthermore, the upcoming Euro 7 regulations will cover a broader range of driving scenarios [9]. This new regulation predictably proposes to extend the temperature limits to −7 °C to 35 °C for moderate conditions and increase the maximum altitude to 1600 m. Extended conditions will cover altitudes up to 2200 m and temperatures ranging from −10 to 45 °C [10]. This strategy addresses the emission challenges of low cold-start temperatures and high summer temperatures across Europe, reflecting the diversity of driving conditions and climates across the continent [11].

Studies demonstrate that extreme environmental conditions, specifically low temperatures and high altitudes, negatively impact ICE performance and exhaust aftertreatment

systems (ATS). The study by Giechaskiel et al. [12] revealed that CO, HC, and NOx emissions from a Euro 6d-Temp gasoline engine doubled at −10 °C compared to mild ambient temperatures during urban driving scenarios, particularly spiking during cold start conditions. The research by Luján et al. [13] showed that low temperatures significantly impacted emissions from a light-duty diesel engine, with CO, HC, and NOx emissions doubling or even tripling during WLTC at −7 °C compared to 20 °C . Also, research by Bermúdez et al. [14] on Euro 4 internal combustion engines and by Suarez-Bertoa et al. [15] analyzing road emissions from three Euro 6d-Temp engines (diesel, gasoline, and hybrid electric gasoline) demonstrated that higher altitudes tend to increase raw emissions of CO and NOx.

In lean ICEs, oxidation catalysts (OCs) are essential for reducing pollutants like CO and HC. The efficiency of these catalysts, however, is influenced by environmental conditions. A study by Serrano et al. [16], examining a Euro 6d-Temp ICE at various altitudes (0 and 2500 m) and temperatures (20 °C and −7 °C), reported increased raw emissions of CO and HC and decreased OC efficiency at 2500 m and −7 °C. Additionally, increased CO and HC raw emissions at higher altitudes led to higher inhibitory effects, damaging OC performance. Historical research, including studies by Voltz et al. [17] and Oh et al. [18], has established that high CO and HC concentrations impair the oxidation process, decreasing conversion efficiency. At low temperatures, the inhibitory effects of CO and HC on oxidation increase [19]. Additionally, research by Lefort et al. [20], utilizing various diesel fuels and operational settings with different CO, HC, and NOx levels, indicated that increased CO concentrations led to higher CO and HC light-off temperatures. However, at high temperatures, the inhibition effect on oxidation declined because of decreased chemisorption. These observations underscored the competitive nature of CO [21] and HC [22] against O_2 for binding to active sites and the critical role of surface intermediates.

Although the presence of H_2 in exhaust gases in lean ICEs is usual, this chemical species has not been given prominence in the study of oxidation catalysts. Nonetheless, with regulatory shifts favouring the adoption of alternative fuels and technologies to decrease CO_2 emissions, H_2 has emerged as a critical element in transitioning towards more sustainable transportation [23]. This shift includes strategies involving H_2 combustion [24] and dual-fuel strategies [25]. Specifically, the dual-fuel H_2 combustion approach has demonstrated substantial gains in fuel efficiency and a general decrease in raw emissions [26]. This enhancement is attributed to the formation of reaction intermediates favoured by the H_2 promotion of hydroxyl radicals (·OH) on the catalyst surface [27]. However, introducing H_2 as a fuel alters the composition of exhaust gases, impacting the operating conditions for ATS. Consequently, a comprehensive assessment of ATS performance is essential to ensuring its effectiveness across various conditions, notably when its efficiency can be affected.

From the previous results obtained in studies on oxidation catalysts under CDC (high altitude in a cold environment) [16] and dual-fuel strategies with H_2 (sea level, room temperature) [28], this study combines both approaches to examine the impact of H_2 on an OC under various environmental conditions in order to study more unfavourable conditions for the catalyst. A simplified reaction mechanism including the primary conversion paths for CO, HC, and H_2 was implemented into a one-dimensional model for multi-layer washcoat honeycomb catalytic converters [29]. The model was calibrated with data from two sets of experimental tests. First, data from a Euro 6d-Temp engine coupled with a MEDAS altitude simulator were used, operating at two distinct conditions: sea level (0 m) and 20 °C, and an altitude of 2500 m at −7 °C in ambient temperature. These data were used as the basis for calibrating the model in the absence of H_2. To assess the impact of H_2, the calibration process integrated selectivities for various reaction pathways derived from temperature ramp tests conducted on diesel exhaust gases with varying concentrations of H_2. The calibrated model was then used to evaluate how H_2 affects the conversion efficiency of CO and HC under the specified environmental conditions, covering a broad spectrum of H_2 concentrations. Furthermore, the study investigated the reactivity of CO and HC along the

catalyst monolith, focusing on the selectivity towards different oxidation pathways. The objective was to understand how H_2 variably influences these reaction pathways in the environmental scenarios studied and to identify the mechanisms behind these differences.

2. Materials and Methods

This work used a combination of experimental and theoretical methods to analyze the effect of H_2 presence in the exhaust gas on the operation of an OC in warm sea-level, high-altitude, and low-temperature conditions. The objective is to provide new insights into the performance of the oxidation catalysts in the presence of H_2, especially under high-altitude conditions resulting in higher pollutant raw emissions.

The study was based on tests conducted by Serrano et al. [16] on an HSDI diesel Euro 6d-Temp engine installed in a test bench coupled with the Horiba MEDAS. These tests provided the baseline data to calibrate the reactions that do not involve H_2 in the OC model. Reactions influenced by the presence of H_2 were calibrated using CO and HC selectivities to different reaction pathways obtained in temperature-ramp tests [28]. After the model calibration, a comprehensive analysis was conducted to assess the impact of H_2 on the conversion efficiency and selectivities of CO and HC reactions along the monolith under both cold altitude and warm sea-level conditions. The analysis covered different molar fractions of H_2 representative of dual-fuel H_2-diesel engine exhaust gases, ranging from 500 ppm to post-injection strategies reaching 10,000 ppm.

2.1. Experimental Setup

The experimental facility used as a base to conduct the model calibration in conventional diesel combustion (CDC) cases consisted of an HSDI diesel Euro 6d-Temp engine for passenger car applications, whose detailed characteristics are described in [16]. The engine was installed on a test bench integrated with Horiba MEDAS. The MEDAS system, an altitude simulator developed by CMT—Thermofluids & Clean Mobility [30,31], facilitated variable ambient pressure for the engine based on the imposed driving altitude. It can handle altitudes from sea level to 5000 m and ambient temperatures from −15 to 45 °C [30]. The ATS comprised a close-coupled OC and a wall-flow particulate filter coated as a selective catalytic reduction system. The characteristics of the OC are listed in Table 1.

Table 1. Characteristics of the oxidation catalyst.

Substrate	Cordierite
Washcoat	Alumina oxide and zeolite
Coating	Pt
Monolith length [mm]	140
Monolith diameter [mm]	120
Channel cross-section	Square
Cell density [cpsi]	400
Cell size [mm]	1.04
Wall thickness [mm]	0.23
Catalytic area [m^2]	3.95

The experiments conducted by Serrano et al. [16] were carried out under steady-state conditions, with the engine operating at constant torque and speed until thermal stabilization was achieved, enabling the measurement of CO and HC conversion efficiencies. These tests were guided by the gas inlet temperature and the exhaust gas mass flow of the OC, which were constrained by the two distinct ambient conditions. To establish a baseline for comparison, the conversion efficiency of pollutants was measured at 0 m of altitude and 20 °C, referred to as the warm sea-level case. This was then compared to the results obtained at 2500 m of altitude, corresponding to an ambient pressure of 0.747 bar and a temperature of −7 °C, referred to as the cold altitude case. To establish the mass flow of exhaust gases, the engine speed was assessed at 1000 rpm, 1250 rpm, and 1500 rpm under warm sea-level conditions. Following this, the speed range was modified

for the cold altitude scenario to achieve a comparable exhaust mass flow in both situations. Additionally, the OC inlet gas temperature was controlled within the same range (100 to 300 °C) for both cases. The exhaust gas mass flow, catalyst inlet pressure, and temperature, along with CO and HC molar fractions at the catalyst inlet for both warm sea-level and cold altitude cases, are detailed in Tables 2 and 3.

Table 2. Input data for 0 m & 20 °C.

Engine Speed [rpm]	OC Inlet Pressure [bar]	Exhaust Gas Mass Flow [kg/h]	OC Inlet Temperature [°C]	CO Inlet Molar Fraction [ppm]	HC Inlet Molar Fraction [ppm]
1000	1.01	41.05	86.8	386	126
1000	1.00	38.89	108.8	343	159
1000	1.00	39.15	116.1	351	131
1000	1.00	38.72	124.4	317	157
1000	1.00	38.75	132.5	254	86
1000	1.01	38.64	159.6	270	137
1000	1.01	39.52	204.4	323	152
1000	1.01	40.29	254.1	473	164
1000	1.02	45.14	306.6	370	113
1250	1.01	51.63	200.0	402	205
1250	1.02	54.02	248.1	536	194
1250	1.03	62.23	305.2	570	141
1475	1.04	65.27	148.7	566	246
1500	1.02	66.00	98.2	649	282
1500	1.03	71.52	207.6	533	210
1500	1.04	76.29	253.2	595	190
1500	1.05	90.25	309.9	367	81

Table 3. Input data for 2500 m & −7 °C.

Engine Speed [rpm]	OC Inlet Pressure [bar]	Exhaust Gas Mass Flow [kg/h]	OC Inlet Temperature [°C]	CO Inlet Molar Fraction [ppm]	HC Inlet Molar Fraction [ppm]
1000	0.76	31.57	99.5	914	512
1000	0.76	33.02	128.1	495	262
1000	0.75	33.57	152.4	423	258
1000	0.76	33.25	181.5	274	196
1000	0.77	35.78	275.6	286	181
1250	0.75	39.49	94.3	1169	836
1250	0.75	42.71	158.1	548	322
1250	0.76	43.22	181.6	411	253
1250	0.76	44.23	220.4	294	221
1250	0.76	52.74	276.0	202	124
1500	0.75	54.22	92.5	1194	838
1500	0.76	58.72	147.6	616	257
1500	0.76	60.33	158.8	461	268
1500	0.76	65.58	207.2	308	175
1500	0.76	67.81	253.0	222	97
1500	0.77	75.07	301.6	198	78
1750	0.76	70.01	126.0	946	468
1750	0.78	72.21	173.0	602	290
1750	0.78	78.31	230.2	384	217
1750	0.78	81.23	278.6	257	154

At each tested point, pollutants were continuously measured according to the specific measurement protocol described in [16].

To examine the effect of H_2 on the OC under warm sea-level and cold altitude cases, modeling results from a previous work by Piqueras et al. [28] were employed. These results analyzed the selectivity of CO and HC reactions to O_2 and ·OH due to the presence of H_2 using a reduced-order model proposed by Piqueras et al. [29]. The selectivities were modeled based on experimental temperature ramp tests carried out by Herreros et al. [32]. These tests involved a Pt-coated OC on alumina, which was placed in a tubular furnace in the by-pass of the exhaust line of a single-cylinder diesel engine. The catalyst inlet gas was doped with varying molar fractions of H_2, ranging from 500 to 8000 ppm. The resulting CO and HC selectivities as a function of the temperature and H_2 inlet molar fraction were integrated into the calibration of the catalyst model utilized in this study.

2.2. Catalyst Model

The study employed a flow-through monolith oxidation catalyst model for dual-layer washcoat, as proposed by Piqueras et al. [29]. This model is part of VATS, a virtual environment developed by CMT-Clean Mobility & Thermofluids to simulate ATS coupled with VEMOD, a gas dynamic software for engine modelling [33]. Detailed descriptions of the model for dual-layer washcoat catalysts can be found in [29], which is based on earlier developments focused on deriving explicit solutions for flow transport in catalytic reactors with single-layer washcoats [34,35] from a 1+1D two-phase approach [36]. The model calculates the concentration of chemical species in the bulk gas along the monolith. It includes convective and diffusive transport mechanisms and accounts for chemical reactivity in dual-layer washcoat structures. The model assumes constant flow properties at the monolith inlet and negligible radial temperature gradients, ensuring consistent behavior across all channels [35], as well as quasi-steady incompressible flow [37,38]. The chemical species conservation equations, corresponding to a single channel bulk gas (Equation (1)) and washcoat layers (Equations (2) and (3)), are written as:

$$u_x \frac{\partial c_g}{\partial x} = -S_{s,g} J_{g,wc_1} \tag{1}$$

$$-\sum_{r_{wc_1}} \nu_{r_{wc_1}} R^m_{r_{wc_1}} = S_{s,wc_1} \left(J_{g,wc_1} - J_{wc_1,wc_2} \right) \tag{2}$$

$$-\sum_{r_{wc_2}} \nu_{r_{wc_2}} R^m_{r_{wc_2}} = S_{s,wc_2} J_{wc_1,wc_2} \tag{3}$$

In the equations, subscripts g, wc_1, and wc_2 denote the bulk gas and the two washcoat layers, respectively. The variable u_x indicates the axial velocity of the gas. The term $R^m_{r_{wc_i}}$ quantifies the reaction rate of an mth-order reaction, and $\nu_{r_{wc_i}}$ are the stoichiometric coefficients, with positive values for products and negative values for reactants. Additionally, S_s refers to the specific surfaces of the gas and each washcoat layer. The terms J_{g,wc_1} and J_{wc_1,wc_2} describe the fluxes at the interface between the gas and the upper washcoat layer and between the upper and lower washcoat layers, respectively [29].

The fundamentals of the explicit solver lie in the dependence of the interfacial fluxes on the species concentration at every phase, as proposed by Ratnakar et al. [38]. The explicit solution obtained to determine the concentration of the chemical species at the outlet of the monolith is given by Equation (4). Constants b and d are functions of specific surfaces, diffusion times, reaction rates, and Sherwood numbers, as detailed in [29].

$$c_{g,out} = \frac{\left(d + bc_{g,in}\right) e^{-S_{s,g} b \tau} - d}{b} \tag{4}$$

In parallel to the solution of chemical species transport, the energy balance in the gas and solid phases is also addressed due to the influence of substrate temperature on reactivity and outlet gas concentration, as detailed in [29].

Regarding the reaction mechanism, which is listed in Table 4, it presents the comprehensive reaction mechanism along with the corresponding rates for each reaction accounted for in every catalyst layer, including kinetic constants (k_i) derived from the Arrhenius equation. This reaction mechanism covers, as baseline, primary processes such as HC adsorption/desorption (R_1 and R_2), CO and HC oxidation with O_2 (R_3 and R_4), and NOx interconversion (R_5 and R_6), detailed in [28]. Although these reactions address catalyst behavior with excess O_2, they lack sensitivity to H_2 presence. By introducing ·OH radicals as intermediates, the influence of H_2 can be covered. Mhadeshwar and Vlachos [27] proposed a microkinetic scheme highlighting the significance of the carboxylic pathway. This pathway involves adsorption and desorption steps for various reaction intermediates with a radical nature, including ·H, ·O, ·OH, ·COOH, and ·HCO [39]. This offers an alternative to direct CO oxidation, involving a two-step reaction route forming ·COOH radicals on Pt surface, represented by reaction R_{11}, as detailed in [28]. A similar radical pathway models the HC light-off temperature reduction [32] via reaction R_{12}. The competitive interaction among species is taken into account through the incorporation of an inhibition term, defined for the oxidation of CO and HC in the presence of O_2 (reactions R_3 and R_4 in Table 4). The inhibition term (G_{ox}) was derived using the expression proposed by Voltz et al. [17] as in [16]. Equilibrium constants of the NOx interconversion reaction ($K_{eq,NOx}$) and the water-gas shift reaction ($K_{eq,water}$) are also included, calculated from the thermodynamic data obtained in [40] and [41], respectively.

Table 4. H_2-OC reaction mechanism.

Reaction	Reaction Expression Rate
Zeolite layer	
$C_nH_m + Zeol \leftrightarrows C_nH_m - Zeol$	$R_1 = k_1 c_{HC}(1-\theta_{HC})$ $R_2 = k_2\theta_{HC}$
Platinum layer	
$CO + \frac{1}{2}O_2 \rightarrow CO_2$	$R_3 = \frac{k_3}{G_{ox}} c_{CO} c_{O_2}$
$C_nH_m + \left(n + \frac{m}{4}\right)O_2 \rightarrow nCO_2 + \left(\frac{m}{2}\right)H_2O$	$R_4 = \frac{k_4}{G_{ox}} c_{HC} c_{O_2}$
$NO + \frac{1}{2}O_2 \leftrightarrow NO_2$	$R_5 = k_5 c_{O_2} c_{NO}$ $R_6 = \frac{k_5}{K_{eq,NOx}} c_{NO_2}$
$H_2 + \frac{1}{2}O_2 \rightarrow H_2O$	$R_7 = k_7 c_{H_2} c_{O_2}$
$H_2 + O_2 + 2Pt \leftrightarrow 2 \cdot OH - Pt$	$R_8 = k_8 c_{O_2} c_{H_2}(1-\theta_{OH})$ $R_9 = k_9\theta_{OH}$
$H_2 + 2 \cdot OH - Pt \rightarrow 2H_2O + 2Pt$	$R_{10} = k_{10} c_{H_2} \theta_{OH}$
$CO + 2 \cdot OH - Pt \rightarrow H_2O + CO_2 + 2Pt$	$R_{11} = k_{11} c_{CO} \theta_{OH}$
$C_nH_m + \cdot OH - Pt + \left(\frac{4n+m-1}{4}\right)O_2 \rightarrow nCO_2 + \left(\frac{m+1}{2}\right)H_2O + Pt$	$R_{12} = k_{12} c_{HC} \theta_{OH}$
$CO + H_2O \leftrightarrow CO_2 + H_2$	$R_{13} = k_{13} c_{CO} c_{H_2O}$ $R_{14} = \frac{k_{13}}{K_{eq,water}} c_{CO_2} c_{H_2}$
$C_nH_m + nH_2O \rightarrow nCO + \left(n + \frac{m}{2}\right)H_2$	$R_{15} = k_{15} c_{HC} c_{H_2O}$

3. Results and Discussion

This section discusses the results obtained from modelling the catalyst to assess the reactivity in the presence of H_2 by applying the methodology detailed in Section 2. First, the methodology used and the results obtained to carry out the calibration of the OC model are presented. The analysis of the results obtained after the model calibration was focused on the study of the reactivity of the CO and the HC in the OC as a function of the H_2 molar fraction under warm sea-level and cold high-altitude conditions. From the OC overall results, the evolution of the selectivity of CO and HC to O_2 and ·OH, HC adsorption, and the conversion efficiency along the cross-section of the monolith were analyzed.

3.1. Modeling H_2 Effect under Altitude and Sea Level Conditions

The initial phase of the study focused on model calibration to reproduce the observed conversion efficiencies for CO and HC during steady-state tests conducted under warm sea-level and cold high-altitude conditions, as described in [16]. The calibration tests are detailed in Tables 2 and 3. In particular, Table 2 displays the experimental data for warm sea-level conditions (0 m and 20 °C), and Table 3 displays those corresponding to cold high-altitude conditions (2500 m and −7 °C).

Due to the absence of H_2 in these tests, the calibration was restricted to reactions excluding this species. Specifically, it focused on HC adsorption and desorption (R_1 and R_2), CO (R_3), and HC (R_4) oxidation reactions in the presence of O_2. The calibration of kinetic constants for these reactions considered the effects of thermal transients on the oxidation and the adsorption-desorption equilibrium, as well as the influence of HC coverage on the reaction rate of the adsorption-desorption dynamics. This methodology facilitated a steady-state representation at test completion, distinguishing between HC oxidation and adsorption conversion efficiencies under varying environmental conditions.

In this initial part of the calibration, the objective function, defined by Equation (5) and minimized using the simplex search method by Lagarias et al. [42], represented the weighted sum of cumulative errors in conversion efficiency (C_{eff}) for CO and HC. It considered the modulus of the error up to each time point (t) for each pollutant species (p).

$$\Phi_{OC_{O_2}} = \sum_{\text{test}} \omega_{\text{test}} \left(\sum_t \varepsilon_{CO}^t + \sum_t \varepsilon_{HC}^t \right) \tag{5}$$

$$\varepsilon_p^t = |C_{eff_{p,exp}} - C_{eff_{p,mod}}| \tag{6}$$

The results of the CO and HC conversion efficiency of the experimental tests for both warm sea-level and cold altitude cases are shown in the contour maps in Figure 1, which is analyzed in detail in [16].

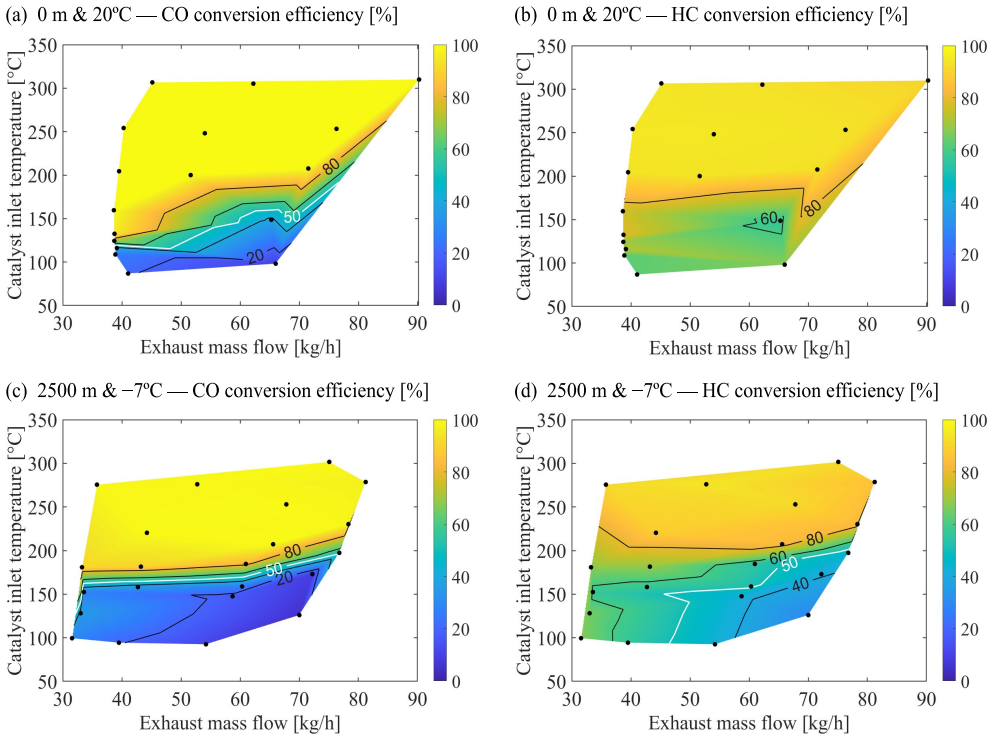

Figure 1. Experimental results for CO and HC conversion efficiency as a function of exhaust mass flow and catalyst inlet temperature for both warm sea-level and cold altitude conditions: (**a**) CO conversion efficiency at 0 m & 20 °C; (**b**) HC conversion efficiency at 0 m & 20 °C; (**c**) CO conversion efficiency at 2500 m & −7 °C; and (**d**) HC conversion efficiency at 2500 m & −7 °C [16].

Figure 2 presents the modeling results of the steady-state tests under warm sea-level and cold high-altitude conditions. The comparison of the model results with experimental data, depicted in Figure 1, points out its ability to simulate CO and HC conversion efficiencies accurately.

The comparison between Figures 1a and 2a evidences how the model is able to capture the CO conversion behavior at the warm-sea level. The model successfully predicted the low reactivity fashion below 100 °C OC inlet temperature. Additionally, it accurately reproduced the enhancement in CO conversion efficiency and its sensitivity to variation in exhaust mass flow as temperature increased. Furthermore, the model identified the threshold in mass flow and temperature where 100% CO conversion was achieved.

Regarding the CO conversion efficiency under cold high-altitude conditions, as illustrated in Figure 2c, the model reflected the changes in conversion efficiency, caused by modifying environmental conditions. Notably, it reproduced the increase in CO light-off temperature and the significant reduction in CO conversion efficiency at reduced exhaust mass flows, a trend more pronounced under cold high-altitude conditions than its warm sea-level counterpart.

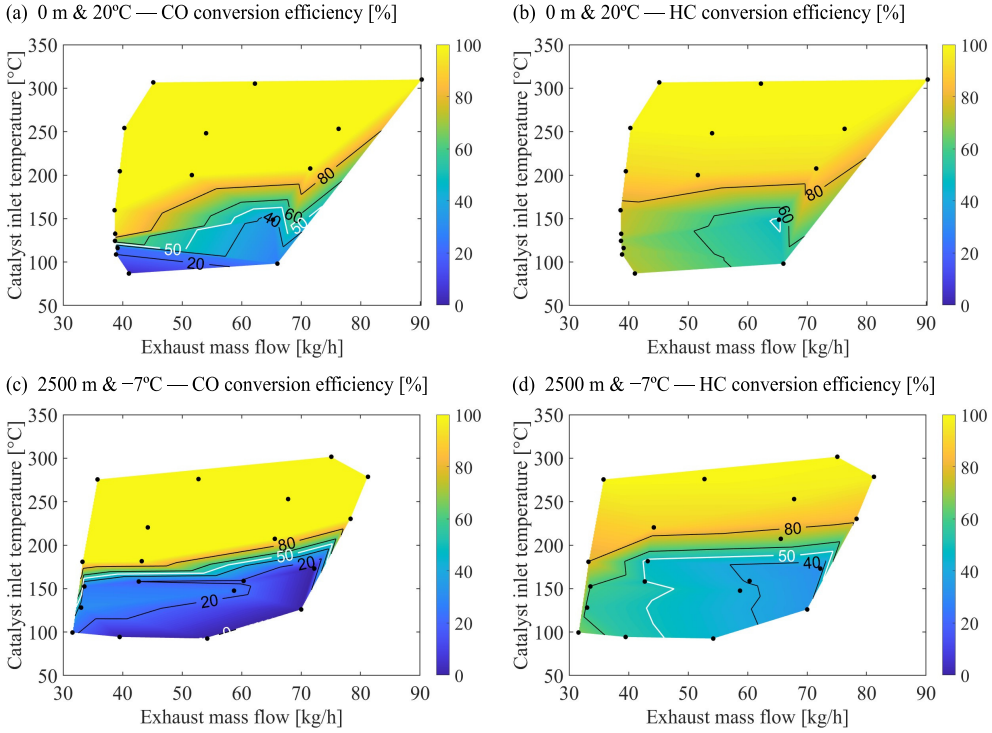

Figure 2. Modeled results for CO and HC conversion efficiency as a function of exhaust mass flow and catalyst inlet temperature: (**a**) CO conversion efficiency at 0 m & 20 °C; (**b**) HC conversion efficiency at 0 m & 20 °C; (**c**) CO conversion efficiency at 2500 m & −7 °C; and, (**d**) HC conversion efficiency at 2500 m & −7 °C.

The ability of the model to predict HC conversion efficiency under varying environmental conditions was further confirmed by comparing Figure 2b,d with their corresponding experimental data (Figure 1b,d). Notably, the model accurately predicted the dominance of zeolite adsorption at lower temperatures [16]. Additionally, it captured the dependence of the conversion efficiency on both temperature and mass flow rate for oxidation reactions. However, the model exhibited lower sensitivity than the experiments to these factors.

The calibrated reactions allowed CO and HC elimination prediction across diverse conditions under CDC operation, emphasizing the O_2 oxidation pathway for lean combustion scenarios and accounting for HC accumulation. Nonetheless, these reactions cannot account for the influence of H_2 present in exhaust gases, as elaborated in Section 2.1.

To address this gap, a targeted calibration of reactions that occur in the presence of H_2 was needed.

Therefore, the next phase of calibration focused on fine-tuning the reactions involving H_2 within the catalyst, specifically targeting reactions R_7 to R_{12} listed in Table 4. The goal was to refine the predictive capability of the model regarding the catalytic processes influenced by H_2. A new objective function for this calibration phase was added to reflect the selectivities (S_{p,R_k}) of CO and HC to reactions involving H_2 and O_2 pathways. These selectivities were detailed in a preceding investigation by Piqueras et al. [28], which examined the reactivity of an OC across different H_2 concentrations in standard conditions. The objective of this calibration step was to ensure that the removal of CO and HC occurred in the presence of H_2. Selectivity, defined in Equation (7), accounts for the contribution of each reaction (Λ_{p,R_r}) to the conversion of the individual species, calculated as the proportion of a change in concentration of a species due to a specific reaction to its total concentration change, which is the sum of all reaction contributions.

$$S_{i,R_k} = \frac{\Lambda_{i,R_k}}{\sum_r \Lambda_{i,R_r}} \tag{7}$$

A new error function was formulated based on the selectivities of each reaction for both the simulation and the reference case, as described in Equation (8):

$$\varepsilon^t_{S_{i,R_k}} = \sum_{test} \left| S^t_{i,R_{k_{OC_{reference}}}} - S^t_{i,R_{k_{OC_{simulation}}}} \right| \tag{8}$$

Equation (9) shows the objective function to calibrate the model when H_2 is present in the exhaust gases. The second term of this equation refers to the selectivity of CO to the oxidation with O_2 (R_3) and the oxidation with ·OH (R_{11}). Complementary, it also accounts for the selectivity of HC to the oxidation with O_2 (R_4) and the oxidation with ·OH (R_{12}).

$$\begin{aligned} \Phi_{OC_{H_2}} = & \sum_{\text{test}} \omega_{\text{test}} \left(\sum_t \varepsilon^t_{CO} + \sum_t \varepsilon^t_{HC} \right) \\ & + \sum_{\text{test}} \omega_{\text{test}} \left(\sum_{\text{test}} e^t_{S_{CO,R_3}} + \sum_{\text{test}} e^t_{S_{CO,R_{11}}} + \sum_{\text{test}} e^t_{S_{HC,R_4}} + \sum_{\text{test}} e^t_{S_{HC,R_{12}}} \right) \end{aligned} \tag{9}$$

The results corresponding to the OC operation with H_2 are shown in Figure 3, which compares the selectivities for CO and HC oxidation via O_2 or ·OH with those reported by Piqueras et al. [28]. As observed, to account for the presence of H_2 in the exhaust gases for the studied OC, closely aligned with the reference.

With respect to CO reactivity, which is depicted in Figure 3a,c, the model exhibited a high degree of consistency with the reference data in terms of selectivity. The selectivity towards ·OH, which is shown in Figure 3c, indicated that at temperatures below 160 °C for low H_2 concentrations and below 200 °C for high H_2 concentrations. Above these temperature thresholds, introducing H_2 led to a decrease in CO selectivity from ·OH to the O_2 oxidation pathway.

Regarding the selectivity of HC oxidation, which is represented in Figure 3b,d, it showed the same type of trend as observed with CO upon the introduction of H_2. However, it did not reach the selectivity levels for the ·OH pathway observed in CO. The influence of H_2 on HC conversion is weaker at low temperatures due to the adsorption role. In parallel, the HC selectivity to the ·OH pathway decreases as temperature does, but this trend is more gradual and less affected by H_2 concentration than for CO.

As a result of this calibration, the kinetic constants collected in Table A1—Appendix A were obtained. These constants include the activation energies and pre-exponential factors of the reactions involved and the accumulation capacity of HC and ·OH in each monolith channel.

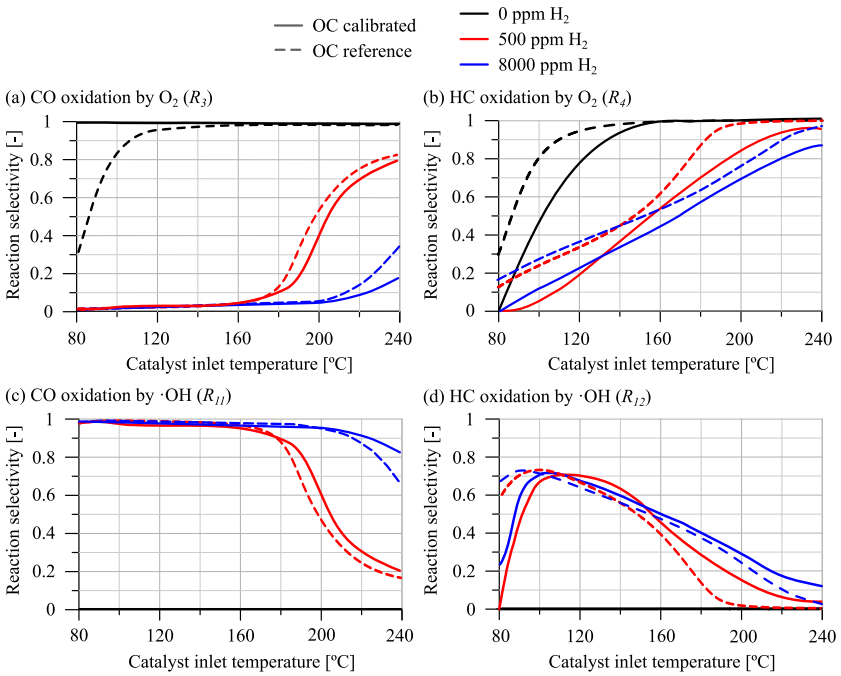

Figure 3. CO and HC selectivity to O_2 and ·OH in OC calibrated and OC reference: (**a**) CO oxidation by O_2; (**b**) HC oxidation by O_2; (**c**) CO oxidation by ·OH; and, (**d**) HC oxidation by ·OH.

3.2. CO Reactivity Analysis

For the CO case, Figure 4 shows the percentage increase in CO conversion efficiency relative to the baseline results shown in Figure 2a under warm sea-level conditions, as a function of the exhaust mass flow and catalyst inlet temperature. Each plot is devoted to 500, 1000, 5000, and 10,000 ppm of H_2 molar fraction into the catalyst inlet gas, as previously detailed in Section 2.

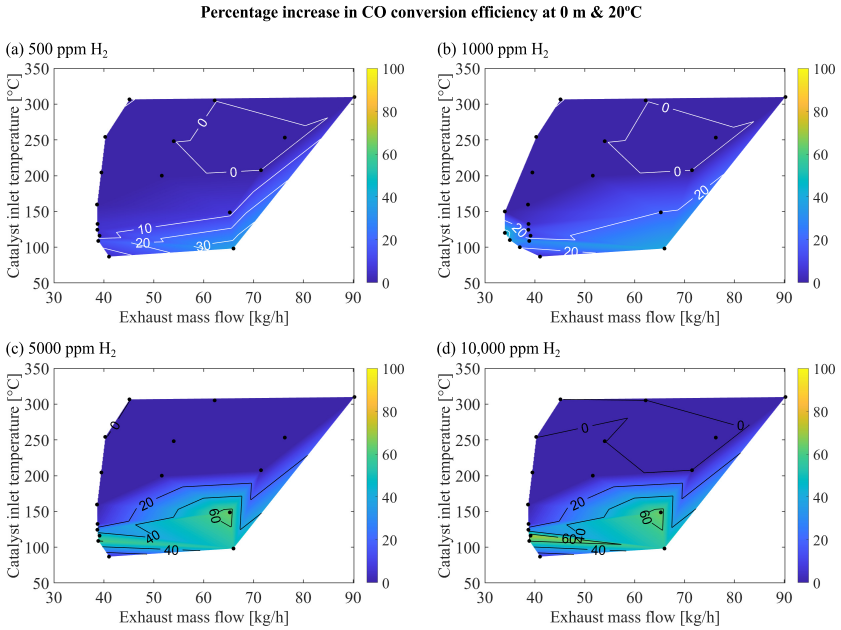

Figure 4. Increase in CO conversion efficiency at 0 m & 20 °C as a function of the exhaust mass flow and catalyst inlet temperature for different H_2 inlet molar fractions: (**a**) 500 ppm; (**b**) 1000 ppm; (**c**) 5000 ppm; and, (**d**) 10,000 ppm.

The findings indicated an enhancement in CO reactivity with increasing molar fractions of H_2, particularly evident within the low-temperature range under low flow condi-

tions (around 100 °C and 35–50 kg/h). This effect extended to higher temperatures as the operating conditions transitioned to higher flow rates (around 150 °C with 60–70 kg/h). The improvement in conversion efficiency was most pronounced in the operating points with low conversion efficiency in the absence of H_2. As shown in Table 2, these points were characterized by elevated CO concentrations and low temperatures, avoiding the oxidation by O_2.

The improvement in CO conversion efficiency consistently increased up to 5000 ppm in the H_2 molar fraction, resulting in a significant improvement above 60% at approximately 150 °C and an exhaust mass flow of 65 kg/h. This substantial increase differed from the 20% improvement observed at 1000 ppm and less than 10% at 500 ppm in H_2 molar fraction, accompanied by an expansion of the enhanced region to higher temperatures. However, the addition of 10,000 ppm of H_2 did not lead to a discernible improvement in reactivity beyond that achieved with 5000 ppm, being the enhancement stabilized at 60%. This trend indicated a saturation point beyond which further increases in H_2 concentration did not significantly impact reactivity.

The effect of introducing H_2 on improving CO conversion efficiency was also observed under cold high-altitude conditions. Figure 5 shows the percentage increase in CO conversion efficiency relative to baseline results shown in Figure 2c, considering cold high-altitude scenarios influenced by exhaust mass flow and catalyst inlet temperature. Similar to the warm sea-level counterpart, the same molar fractions of H_2 were introduced into the catalyst inlet gas. An enhancement band was observed at 150 °C in the low-to-mid mass flow range (30–60 kg/h) for the cases of 1000, 5000, and 10,000 ppm of H_2 molar fraction. In contrast to the warm sea-level case, introducing 10,000 ppm further extends this band to the highest mass flow rates (70–80 kg/h).

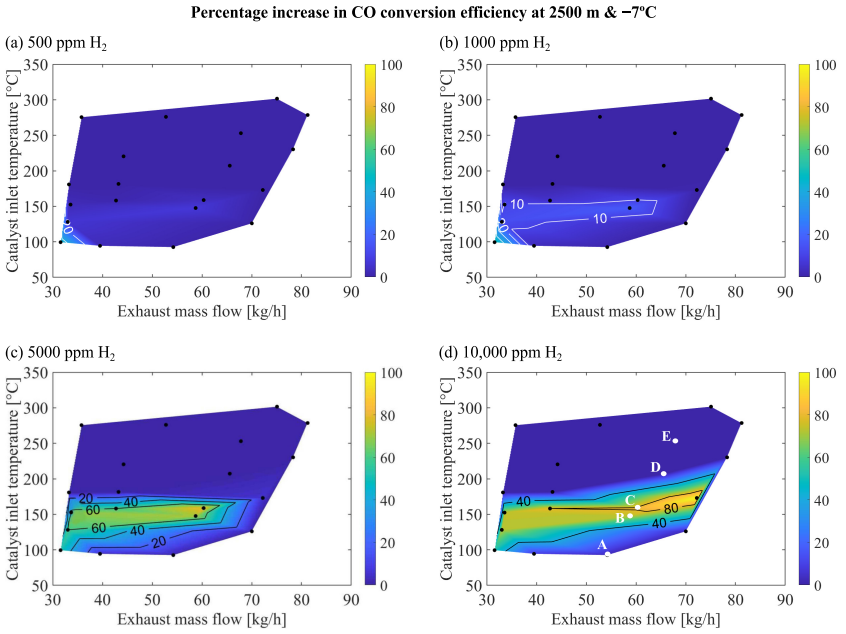

Figure 5. Increase in CO conversion efficiency at 2500 m & −7 °C as a function of the exhaust mass flow and catalyst inlet temperature for different H_2 inlet molar fractions: (**a**) 500 ppm; (**b**) 1000 ppm; (**c**) 5000 ppm; and (**d**) 10,000 ppm.

The difference in the increase in CO conversion efficiency profiles with respect to the warm sea-level case was primarily attributed to high CO raw concentration in cold high-altitude conditions (see Table 3). This limited the effectiveness of H_2 in enhancing CO reactivity. At lower molar fractions of H_2, such as 500 ppm, the enhancement in conversion efficiency was negligible and limited to regions with low exhaust mass flow and temperature, where the concentration of CO and inhibition were reduced. However, as the H_2 molar fraction increased, the enhancement region shifted towards higher exhaust mass

flows, highlighting the role of the ·OH reaction pathway and the decrease in inhibition caused by CO consumption due to this carboxylic pathway. Higher H_2 molar fractions made this effect increasingly apparent. Unlike warm sea-level conditions, high molar fractions of H_2 did not lead to saturation effects in cold high-altitude conditions at every operating point due to the inherently lower initial reactivity of the catalyst in the absence of H_2. Therefore, significantly greater reactivity was observed when the H_2 molar fraction was increased from 5000 to 10,000 ppm, especially in areas of high mass flow, which were highly affected by inhibition under CDC operation.

To elucidate the improvement in CO reactivity observed in the regions depicted in Figures 4 and 5 and to understand the variability in the response to H_2 introduction across different operating points, the analysis of the axial distribution of conversion efficiency throughout the catalyst was assessed. This involved identifying the regions of the OC that exhibited the highest reactivity at each operating point, as well as those areas most affected by the introduction of H_2. For this purpose, three sections along the length of the monolith were selected. First, the catalyst inlet cross-section corresponds to 4.66 mm from the inlet of the monolith. Then, the middle cross-section was 69.99 mm, and the outlet cross-section was 135.34 mm. The study prioritizes the cold high-altitude case for a more detailed examination, given its more notable increase in reactivity attributed to higher levels of inhibition under CDC operation. Table 5 presents points A-E from Figure 5 as representative of operating points corresponding to the region where a significant increase in reactivity was observed upon introducing H_2. These points are arranged in increasing order regarding inlet gas temperature and exhaust mass flow to the OC.

Table 5. Selected points for 2500 m & −7 °C conditions.

Point	Exhaust Mass Flow [kg/h]	OC Inlet Temperature [°C]	CO Inlet Molar Fraction [ppm]	HC Inlet Molar Fraction [ppm]
A	54	92.5	1194	838
B	59	147.6	616	257
C	60	158.8	461	268
D	66	207.2	308	175
E	68	253.0	222	97

Thus, Figure 6 presents the axial distribution of CO conversion efficiency along the monolith length for points A–E. Each subplot within Figure 6 corresponds to a different H_2 molar fraction at the catalyst inlet gas. The results for the CDC operation are shown in Figure 6a revealed three different trends across the five operational points considered. At operating point A, no reactivity was observed across any section of the monolith due to the low inlet gas temperature (93 °C) and very high CO molar fraction (1194 ppm), resulting in significant inhibition. Points B and C exhibited higher inlet gas temperatures but also high CO molar fractions (616 ppm and 461 ppm, respectively). In these cases, some reactivity was observed, increasing along the monolith. As CO started to react at the inlet region of the monolith, its concentration decreased, thereby reducing inhibition in subsequent regions and enhancing overall reactivity along the monolith. In these scenarios, the entire length of the monolith contributed to the reaction, and an expanded catalyst volume would enhance CO conversion efficiency. Finally, points D and E, characterized by high inlet gas temperatures and low CO concentrations (low inhibition), demonstrated conversion efficiencies near 100%, with most conversion occurring at the inlet cross-section of the monolith.

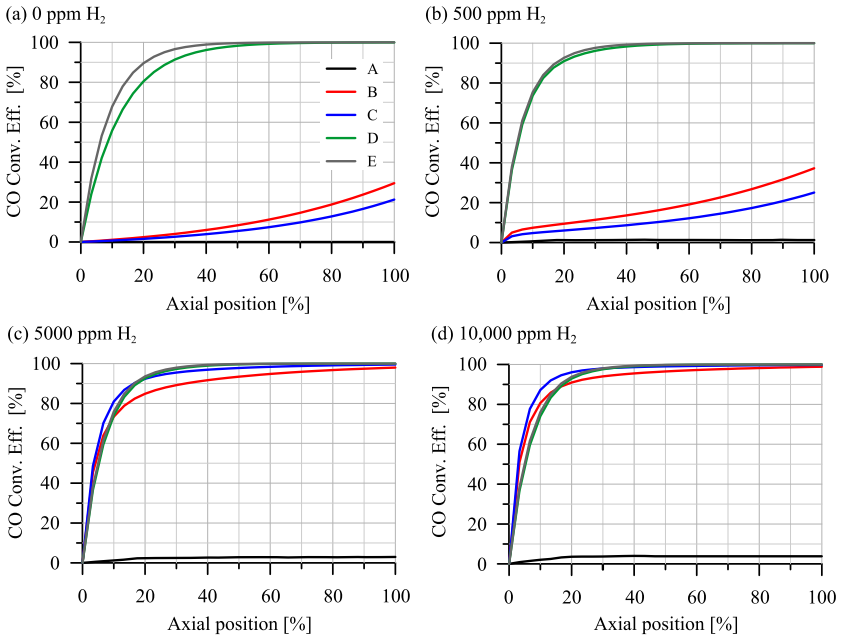

Figure 6. Axial distribution of CO conversion efficiency with different H_2 molar fractions for 2500 m & −7 °C and points A, B, C, D, and E from Table 5: (**a**) 0 ppm; (**b**) 500 ppm; (**c**) 5000 ppm; and (**d**) 10,000 ppm.

Upon introducing 500 ppm in the H_2 molar fraction, as shown in Figure 6b, the conversion efficiency resulted largely consistent with the CDC scenario. Only minor differences at points B and C, with only a marginal increase in conversion efficiency in the initial cross-section of the monolith, contributed to increasing the reactivity along the whole monolith due to the early inhibition decrease. This enhanced conversion efficiency in the inlet region is attributed to the reaction pathways enabled by the presence of H_2, particularly through the formation of ·OH radicals on the catalytic surface. At this relatively low H_2 concentration, the generation of these surface groups was limited, resulting in only a modest reactivity increase at the monolith inlet. Points D and E also experienced a boost in reactivity from the H_2 presence at the inlet, with point D showing slightly higher reactivity. Compared to point E, it resulted in greater conversion efficiency due to its lower inlet mass flow and, hence, longer residence time. However, since both points already achieved near 100% conversion efficiency, no significant improvement was noted in the overall conversion efficiency increase map (Figure 5a).

The enhancement effects were more pronounced when the H_2 molar fraction was increased to 5000 and 10,000 ppm, as illustrated in Figure 6c,d. At points B and C, the increase in reactivity resulting from the high molar fraction of H_2 led to greater availability of ·OH radicals at the monolith inlet, consequently increasing the conversion efficiency to near 100% in these inlet regions. For operating points D and E, the enhanced reactivity improved conversion efficiency in the inlet region, but only marginally, as these points already face limitations due to mass transfer rather than reactivity. Furthermore, the elevated availability of ·OH radicals with this high H_2 concentration promoted certain reactivity even at operating point A, despite its low temperature.

The findings depicted in Figure 6 demonstrated that H_2 predominantly influences the inlet cross-section of the monolith, with the observed variations in reactivity in subsequent sections resulting from alterations in CO concentration initiated in these inlet cross-sections. To understand why the impact of H_2 presence was primarily taking place at the inlet of the monolith, it is crucial to examine the selectivity of CO reactions with O_2 and ·OH across different operating points and cross-sections of the monolith. Figure 7 represents the selectivity of CO to ·OH in the context of cold high-altitude conditions with 500 ppm

(Figure 7a,b) and 10,000 ppm (Figure 7c,d) in H_2 molar fraction, at the inlet and medium cross-sections of the monolith.

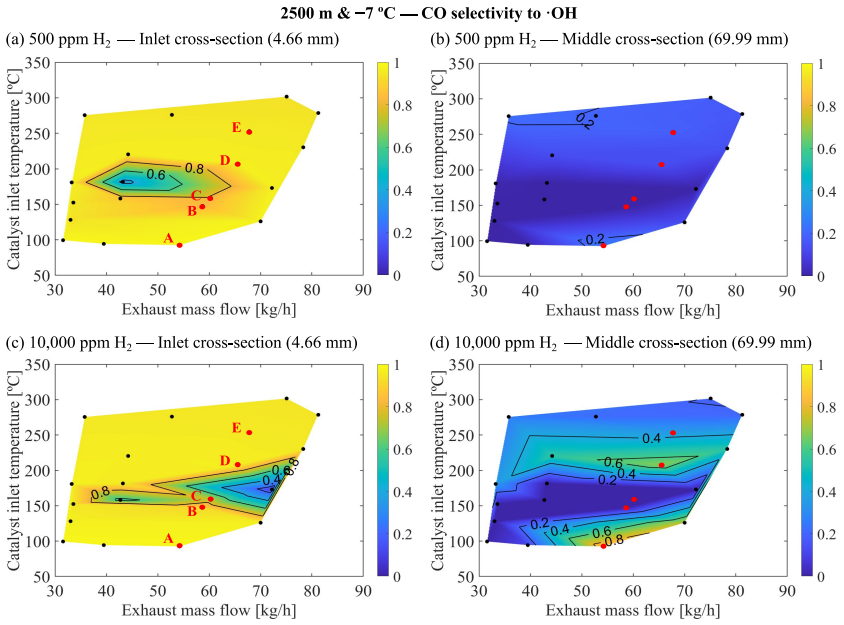

Figure 7. Axial distribution of CO selectivity to ·OH along the cross-section of the monolith at 2500 m & −7 °C as a function of the exhaust mass flow and catalyst inlet temperature for 500 and 10,000 ppm in H_2 molar fraction: (**a**) 500 ppm—Inlet cross-section; (**b**) 500 ppm—Middle cross-section; (**c**) 10,000 ppm—Inlet cross-section; and (**d**) 10,000 ppm—Middle cross-section.

The reactivity of CO with ·OH varied significantly between the inlet and middle cross-sections. In particular, the selectivity to CO with ·OH was considerably higher in the inlet cross-section of the monolith for 500 ppm and 10,000 ppm in the H_2 molar fraction, approaching a value of 1 for most operating points, except in areas showing the most significant increases in conversion efficiency. This selectivity sharply declined along the monolith length, with much lower values in the middle cross-sections, reaching its peak at approximately 60% for 500 ppm and 80% for 10,000 ppm. These peaks in CO selectivity to ·OH occurred in regions with minimal increases in conversion efficiency. The areas of high selectivity in the middle cross-section aligned with areas of low temperature where there was no reactivity (point A) and, to a lesser degree, with areas of high temperature where conversion efficiency was already elevated without H_2 (points D and E). In both scenarios, reactivity in these areas remained low due to unfavourable conditions that avoided oxidation (point A) or oxidation that had already occurred in the inlet cross-section, leaving no residual CO to react (points D and E). This selectivity pattern may seem counterintuitive since the zones with the most pronounced improvements in conversion efficiency, namely points B and C, upon H_2 introduction, appeared least affected by the CO with ·OH reaction pathway. Moreover, the selectivity for this reaction was more significant with 500 ppm in the H_2 molar fraction than with 10,000 ppm.

This seemingly contradictory behavior can be elucidated by examining the interplay between oxidation reactions and inhibition dynamics, alongside the ·OH coverage, as guided by Figure 8. This figure illustrates ·OH coverage at both 500 and 10,000 ppm, focusing on the inlet and middle cross-sections of the monolith under cold high-altitude conditions. At points D and E, the CO conversion efficiency was initially high even under CDC operation. Therefore, the presence of H_2 in the exhaust gases did not alter significantly the reactivity with O_2. Consequently, as observed in Figure 8a, the relatively abundance of H_2 allowed for significant ·OH coverage.

However, at points B and C, the introduction of 500 ppm in the H_2 molar fraction enhanced the CO reactivity via the ·OH pathway. Yet, this H_2 concentration was insufficient

to sustain high ·OH coverages, limiting the reaction rate, particularly in the inlet cross-section, as shown in Figure 8a. With 10,000 ppm in H_2 molar fraction, the ability to generate and maintain ·OH coverage improved significantly in the inlet section (Figure 8c), leading to a substantial increase in CO concentration and decreased inhibition, thus facilitating the oxidation via the O_2 pathway towards the rear end of the monolith. This resulted in high activity but low selectivity for the ·OH reaction, as shown in Figure 7d.

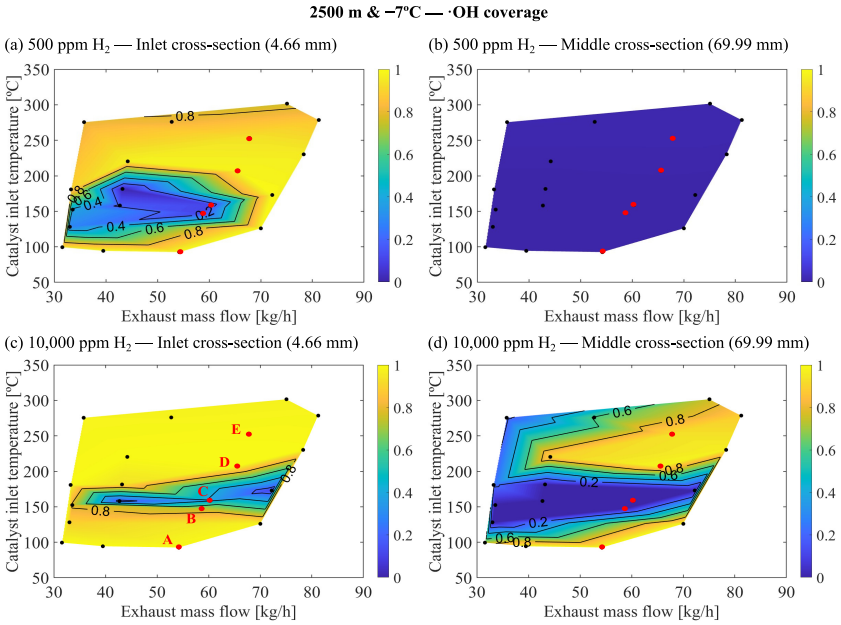

Figure 8. Axial distribution of ·OH coverage along the cross-section of the monolith at 2500 m & −7 °C as a function of the exhaust mass flow and catalyst inlet temperature for 500 ppm and 10,000 ppm in H_2 molar fraction: (**a**) 500 ppm—Inlet cross-section; (**b**) 500 ppm—Middle cross-section; (**c**) 10,000 ppm—Inlet cross-section; and (**d**) 10,000 ppm—Middle cross-section.

After analyzing all cases, it was found that there is a significant correlation between the ·OH coverage and selectivity to this species, confirming that in operating points where conversion efficiency improved, most notably under cold high-altitude conditions, the reaction rate was limited by the capability to stabilize ·OH coverage. This explains why no saturation in conversion efficiency enhancement was observed with higher H_2 molar fractions at altitude. With 10,000 ppm of H_2, the CO selectivity to ·OH was not saturated, indicating a higher selectivity for reactions with O_2. However, the reaction with ·OH effectively reduced CO enough to decrease inhibition, thereby enabling reactivity with O_2 and achieving high CO conversion efficiency.

Moreover, at high temperatures, ·OH coverage neared saturation at the inlet. These areas did not benefit from further H_2 introduction. Conversely, low-temperature regions also reached ·OH saturation, but the prevailing temperatures were too low for significant reactivity, hence not benefiting from increased H_2 concentration. Therefore, it is evident that certain operating points do not gain from H_2, whereas those that do require higher H_2 molar fractions for cold high-altitude conditions compared to warm sea-level conditions. This is mainly due to the higher CO molar fractions in these conditions, which necessitated higher H_2 molar fractions to stabilize sufficient ·OH coverage to guarantee the abatement of CO.

3.3. HC Reactivity Analysis

As regards the impact of H_2 on HC reactivity, Figure 9 shows an improvement in HC conversion efficiency under warm sea-level and cold high-altitude scenarios. This figure illustrates the percentage increase in HC conversion efficiency as a function of the mass flow rate of exhaust gas and the inlet temperature, particularly at high molar fractions

of H_2 (5000 and 10,000 ppm). It is observed that the most significant enhancements in HC conversion efficiency induced by H_2 corresponded with the conditions that were also the most affected by H_2 in terms of CO conversion efficiency, specifically at temperatures around 140 °C–150 °C and an exhaust mass flow ranging between 60 and 65 kg/h. However, in the case of HC, this improvement was less significant, as it aligned with zones where adsorption was dominant in the absence of H_2, leading to moderate HC conversion efficiencies, as shown in Figure 2b,d.

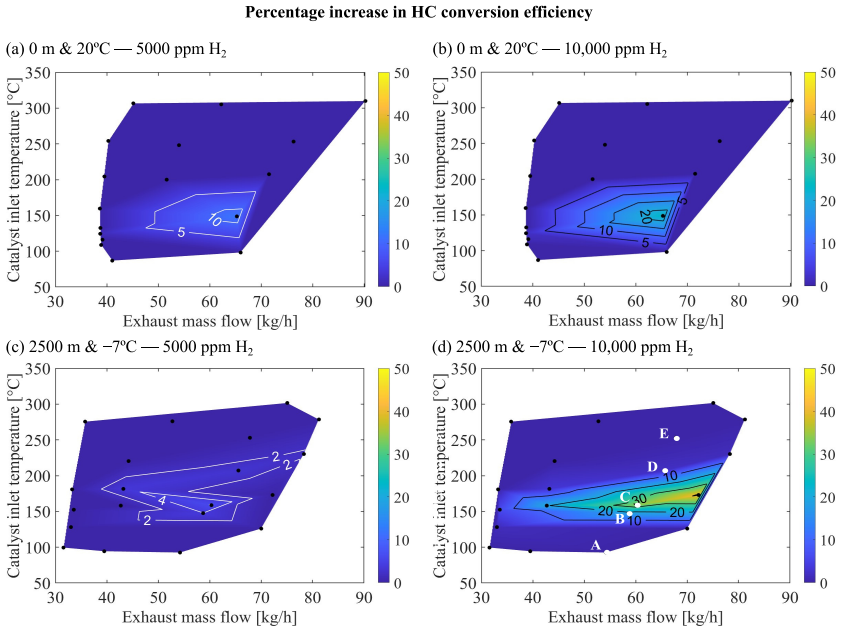

Figure 9. Increase in HC conversion efficiency at 0 m & 20 °C and 2500 m & −7 °C as a function of the exhaust mass flow and catalyst inlet temperature for different H_2 inlet molar fractions: (**a**) 0 m & 20 °C—5000 ppm; (**b**) 0 m & 20 °C—10,000 ppm; (**c**) 2500 m & −7 °C—5000 ppm; and, (**d**) 2500 m & −7 °C—10,000 ppm.

Moreover, introducing H_2 gradually increased the HC conversion under warm sea levels. This was manifested by the fact that introducing 5000 ppm in the H_2 molar fraction (Figure 9a) led to maximum improvements of around 10%, while introducing 10,000 ppm resulted in a maximum improvement exceeding 20%. On the other hand, in cold high-altitude conditions, the enhancement was only relevant with the introduction of 10,000 ppm of H_2, as shown in Figure 9d, with conversion efficiency improvements exceeding 30% at point B, whereas introducing 5000 ppm (Figure 9c) yields only negligible impact (maximum improvement of around 5%).

These results indicate that the impact of H_2 on HC required a higher H_2 molar fraction than in the CO case. It can be attributed to two complementary factors. Firstly, increased reactivity was facilitated by the reaction pathway between HC and ·OH, according to reaction R_{12} detailed in Table 4. Given the inherently lower reactivity of HC compared to CO, significant coverage of ·OH was required, requiring higher molar fractions of H_2. Secondly, greater efficiency in the CO conversion reaction reduced the inhibition caused by this species, facilitating the oxidation of HC with O_2 [16].

Finally, the fact that the improvement in the efficiency of the HC reaction was more moderate compared to that of CO was because H_2 promoted the HC oxidation but in parallel to the adsorption process, which still played a relevant role. This replacement of one reaction mechanism by another was reflected in the selectivity to the HC adsorption, which is depicted in Figure 10 for warm sea-level conditions with 0 ppm of H_2 (plot a) and with 10,000 ppm of H_2 (plot b), and for cold high-altitude conditions with 0 ppm of H_2 (plot c) and with 10,000 ppm of H_2 (plot d).

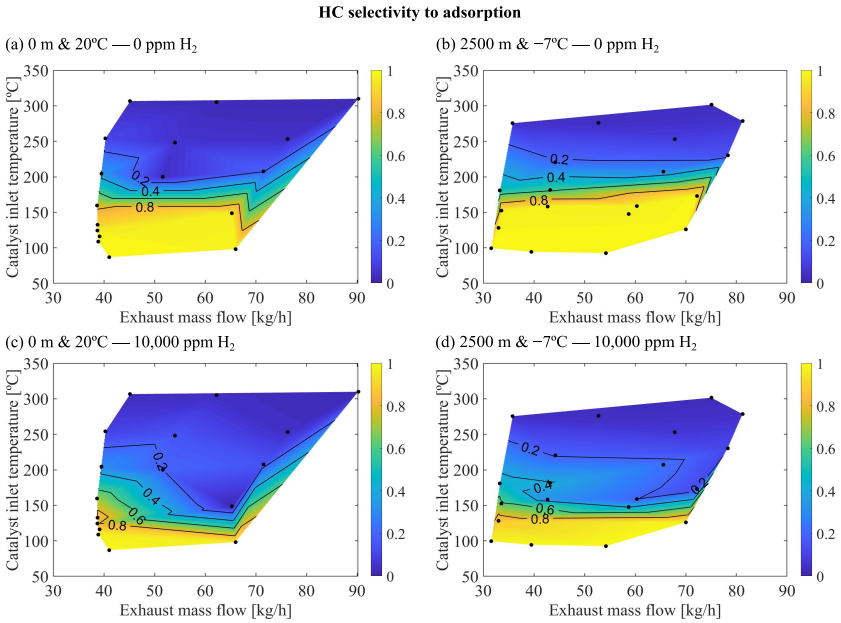

Figure 10. HC selectivity to adsorption as a function of the exhaust mass flow and catalyst inlet temperature for 0 and 10,000 ppm in H_2 molar fraction at different ambient conditions: (**a**) 0 ppm—0 m & 20 °C; (**b**) 0 ppm—2500 m & −7 °C; (**c**) 10,000 ppm—0 m & 20 °C; and, (**d**) 10,000 ppm—2500 m & −7 °C.

The analysis of Figure 10 showed a decrease in the selectivity for adsorption in HC upon the introduction of H_2. When 10,000 ppm of H_2 were introduced, the selectivity adsorption significantly decreased in the area with temperatures around 140–150 °C and exhaust mass flow of 60 to 65 kg/h, falling from 100% with 0 ppm of H_2 in both environmental conditions to 2% with 10,000 ppm of H_2 for the warm sea-level case and to 39% for the cold high-altitude case. This replacement of adsorption by ·OH oxidation was the most significant phenomenon related to the effect of H_2 on the HC conversion, not implying a particularly relevant change in the overall HC conversion efficiency.

4. Conclusions

In this work, the reactivity of an OC was investigated in the presence of H_2 under high-altitude and low-temperature conditions. Combining experimental and modeling techniques, the research extended the conventional reaction mechanism to include alternative CO and HC oxidation pathways based on the formation of ·OH at the active sites of the catalyst. This reaction mechanism was incorporated into a dual-layer washcoat catalyst model sensitive to varying H_2 molar fractions on the CO and HC reactivity. The robustness of the model was validated against experimental data, accurately reflecting CO and HC conversion efficiencies across various environmental conditions. Introducing H_2 highly enhanced CO conversion efficiencies at specific temperature ranges and mass flow rates. At warm sea level, an optimal H_2 molar fraction of 5000 ppm was identified, beyond which no further benefits were observed. However, in cold high-altitude conditions, improvements were evident even with 10,000 ppm in H_2 molar fraction. A detailed analysis revealed that the greatest enhancement in reactivity due to H_2 occurred in the inlet regions of the monolith, primarily attributed to reactions with ·OH radicals. Additionally, a significant portion of the reactivity comes from the O_2 pathway, promoted by the reduction in CO molar fraction resulting from the ·OH pathway. In the case of HC, the lower selectivity of ·OH for this species, combined with its higher conversion at low temperatures due to the adsorption mechanism, results in a less pronounced improvement in HC conversion efficiency upon introducing H_2. This improvement was observed but required higher H_2 molar fractions at the inlet.

The impact of H_2 concentration on conversion efficiency was closely related to operational and environmental factors. Extremely low exhaust temperature conditions, below 100 °C, did not benefit from H_2-induced reactivity enhancement. However, points with higher temperatures and moderate CO concentrations did benefit, with warm sea-level conditions requiring lower H_2 molar fractions than cold high-altitude conditions. Thus, it's advisable to adjust H_2 levels in the exhaust as a function of the engine operating conditions and ambient boundaries, avoiding its presence at low engine demand where it's ineffective and increasing it as ambient temperature decreases and altitude increases.

Author Contributions: Conceptualization, J.R.S. and P.P.; Methodology, P.P. and C.C.; Software, E.J.S. and C.C.; Formal analysis, P.P. and E.J.S.; Investigation, J.R.S., P.P., E.J.S., and C.C.; Resources, J.R.S.; Writing—original draft preparation, P.P., E.J.S., and C.C.; Writing—review and editing, J.R.S., P.P., E.J.S., and C.C.; Supervision, J.R.S. and P.P.; Project administration, J.R.S. and P.P.; Funding acquisition, J.R.S. and P.P. All authors have read and agreed to the published version of the manuscript.

Funding: This research has been supported by Grant PID2020-114289RB-I00 funded by the Spanish Ministerio de Ciencia e Innovación, Agencia Estatal de Investigación (MCIN/AEI/10.13039/501100011033). Additionally, C. Conde thanks PhD funding from Universitat Politécnica de Valéncia through grant FPI-2022-S2-49099, which is supported by project CIPROM/2021/061 funded by Generalitat Valenciana.

Data Availability Statement: Dataset available on request from the authors

Conflicts of Interest: The authors declare no conflicts of interest.

Abbreviations

The following abbreviations are used in this manuscript:

Acronyms	
1D	One dimensional
ATS	Aftertreatment system
CDC	Conventional diesel combustion
ICE	Internal combustion engine
MEDAS	Multifunctional efficient dynamic altitude simulator
OC	Oxidation catalyst
RDE	Real driving emissions
SCRf	Wall-flow articulate filter with selective catalytic reduction
WLTC	Worldwide Harmonized Light Duty Test Cycle
WLTP	Worldwide Harmonized Light Vehicle Test Procedure
Latin Letters	
b	Constant in concentration solution
c	Concentration
C_{eff}	Conversion efficiency
d	Constant in concentration solution
e	Relative cumulative error
G_{ox}	Inhibition term
J	Interfacial flux
k	Arrhenius kinetic constant
$K_{eq,NOx}$	NOx interconversion reaction equilibrium constant
$K_{eq,water}$	Water gas shift reaction equilibrium constant
R	Reaction rate
S	Selectivity
S_s	Specific surface
t	Time
T	Temperature

u	Velocity
wc	Washcoat
x	Axial direction
$Zeol$	Zeolite
Greek letters	
Δ	Variation
ε	Modulus of conversion efficiency error
Λ	Contribution
Φ	Objective function
ν	Stoichiometric coefficient
τ	Residence time
θ	Surface coverage
ω	Weight coefficient
Subscripts	
a	Axial
exp	Experimental
g	gas
i	Phase (g, wc_1, wc_2)
in	Inlet
H_2	Referred to second part of the calibration procedure
k	Index
mod	Modeled
m	Number of H atoms in HC species
n	Number of C atoms in HC species
out	Outlet
O_2	Referred to first part of the calibration procedure
p	Chemical species
w	Wall
wc	Washcoat
Superscript	
m	Reaction order
t	Time

Appendix A

This appendix includes Table A1 with the pre-exponential factors and activation energies of the reactions from Table 4 obtained from the model calibration.

Table A1. Calibration parameters.

Reaction	Pre-Exponential Factors [-]	Activation Energy [kJ/mol]
1	1.05×10^{2}	0
2	2.98×10^{12}	101,000
3	2.48×10^{15}	84,800
4	7.31×10^{14}	92,000
5	6.55×10^{7}	41,000
6	9.67×10^{6}	45,600
7	6.09×10^{14}	78,400
8	6.09×10^{14}	78,400
9	5.00×10^{10}	60,000
10	1.01×10^{8}	81,200
11	1.10×10^{15}	71,800
12	5.96×10^{13}	71,800
13	3.80×10^{9}	88,000
14	4.6×10^{8}	107,100
HC maximum capacity [mol/#]	5.0×10^{-5}	
OH maximum capacity [mol/#]	5.0×10^{-5}	

References

1. Claßen, J.; Pischinger, S.; Krysmon, S.; Sterlepper, S.; Dorscheidt, F.; Doucet, M.; Reuber, C.; Görgen, M.; Scharf, J.; Nijs, M.; et al. Statistically supported real driving emission calibration: Using cycle generation to provide vehicle-specific and statistically representative test scenarios for Euro 7. *Int. J. Engine Res.* **2020**, *21*, 1783–1799. [CrossRef]
2. Ravi, S.S.; Osipov, S.; Turner, J.W. Impact of Modern Vehicular Technologies and Emission Regulations on Improving Global Air Quality. *Atmosphere* **2023**, *14*, 1164. [CrossRef]
3. Tang, G.; Wang, S.; Du, B.; Cui, L.; Huang, Y.; Xiao, W. Study on pollutant emission characteristics of different types of diesel vehicles during actual road cold start. *Sci. Total Environ.* **2022**, *823*, 153598. [CrossRef] [PubMed]
4. Shahariar, G.H.; Sajjad, M.; Suara, K.A.; Jahirul, M.; Chu-Van, T.; Ristovski, Z.; Brown, R.J.; Bodisco, T.A. On-road CO_2 and NOx emissions of a diesel vehicle in urban traffic. *Transp. Res. Part D Transp. Environ.* **2022**, *107*, 103326. [CrossRef]
5. Liu, J.; Li, Y.; Zhang, C.; Liu, Z. The effect of high altitude environment on diesel engine performance: Comparison of engine operations in Hangzhou, Kunming and Lhasa cities. *Chemosphere* **2022**, *309*, 136621. [CrossRef] [PubMed]
6. Selleri, T.; Gioria, R.; Melas, A.D.; Giechaskiel, B.; Forloni, F.; Mendoza Villafuerte, P.; Demuynck, J.; Bosteels, D.; Wilkes, T.; Simons, O.; et al. Measuring Emissions from a Demonstrator Heavy-Duty Diesel Vehicle under Real-World Conditions—Moving Forward to Euro VII. *Catalysts* **2022**, *12*, 184. [CrossRef]
7. Wang, Y.; Hao, C.; Ge, Y.; Hao, L.; Tan, J.; Wang, X.; Zhang, P.; Wang, Y.; Tian, W.; Lin, Z.; et al. Fuel consumption and emission performance from light-duty conventional/hybrid-electric vehicles over different cycles and real driving tests. *Fuel* **2020**, *278*, 118340. [CrossRef]
8. EUR-Lex. Commission Regulation (EU) 2017/1151 of 1 June 2017 Supplementing Regulation (EC) No 715/2007 of the European Parliament and of the Council on Type-Approval of Motor Vehicles with Respect to Emissions from Light Passenger and Commercial Vehicles (Euro 5 and Euro 6) and on Access to Vehicle Repair and Maintenance Information, Amending Directive 2007/46/EC of the European Parliament and of the Council, Commission Regulation (EC) No 692/2008 and Commission Regulation (EU) No 1230/2012 and Repealing Commission Regulation (EC) No 692/2008. 2017. Available online: https://eur-lex.europa.eu/eli/reg/2017/1151/oj (accessed on 14 February 2024).
9. European Commision Questions and Answers: Commission Proposal on the New Euro 7 Standards. 2022. Available online: https://ec.europa.eu/commission/presscorner/detail/en/QANDA_22_6496 (accessed on 20 April 2024).
10. European Commission; Directorate-General for Internal Market, Industry and SMEs. *Technical Studies for the Development of Euro 7—Testing, Pollutants and Emission Limits*; Publications Office of the European Union: Luxembourg, 2022. [CrossRef]
11. Liu, X.; Lara, R.; Dufresne, M.; Wu, L.; Zhang, X.; Wang, T.; Monge, M.; Reche, C.; Di Leo, A.; Lanzani, G.; et al. Variability of ambient air ammonia in urban Europe (Finland, France, Italy, Spain, and the UK). *Environ. Int.* **2024**, *185*, 108519. [CrossRef] [PubMed]
12. Giechaskiel, B.; Valverde, V.; Kontses, A.; Suarez-Bertoa, R.; Selleri, T.; Melas, A.; Otura, M.; Ferrarese, C.; Martini, G.; Balazs, A.; et al. Effect of extreme temperatures and driving conditions on gaseous pollutants of a Euro 6d-Temp gasoline vehicle. *Atmosphere* **2021**, *12*, 1011. [CrossRef]
13. Luján, J.M.; Climent, H.; Ruiz, S.; Moratal, A. Influence of ambient temperature on diesel engine raw pollutants and fuel consumption in different driving cycles. *Int. J. Engine Res.* **2019**, *20*, 877–888. [CrossRef]
14. Bermúdez, V.; Serrano, J.R.; Piqueras, P.; Gómez, J.; Bender, S. Analysis of the role of altitude on diesel engine performance and emissions using an atmosphere simulator. *Int. J. Engine Res.* **2017**, *18*, 105–117. [CrossRef]
15. Suarez-Bertoa, R.; Valverde, V.; Pavlovic, J.; Clairotte, M.; Selleri, T.; Franco, V.; Kregar, Z.; Astorga, C. On-road emissions of Euro 6d-TEMP passenger cars on Alpine routes during the winter period. *Environ. Sci. Atmos.* **2021**, *1*, 125–139. [CrossRef]
16. Serrano, J.R.; Piqueras, P.; Sanchis, E.J.; Diesel, B. Analysis of the driving altitude and ambient temperature impact on the conversion efficiency of oxidation catalysts. *Appl. Sci.* **2021**, *11*, 1283. [CrossRef]
17. Voltz, S.E.; Morgan, C.R.; Liederman, D.; Jacob, S.M. Kinetic Study of Carbon Monoxide and Propylene Oxidation on Platinum Catalysts. *Ind. Eng. Chem. Prod. Res. Dev.* **1973**, *12*, 294–301. [CrossRef]
18. Oh, S.H.; Cavendish, J.C. Transients of Monolithic Catalytic Converters: Response to Step Changes in Feedstream Temperature as Related to Controlling Automobile Emissions. *Ind. Eng. Chem. Prod. Res. Dev.* **1982**, *21*, 29–37. [CrossRef]
19. Datye, A.K.; Votsmeier, M. Opportunities and challenges in the development of advanced materials for emission control catalysts. *Nat. Mater.* **2021**, *20*, 1049–1059. [CrossRef] [PubMed]
20. Lefort, I.; Herreros, J.M.; Tsolakis, A. Reduction of Low Temperature Engine Pollutants by Understanding the Exhaust Species Interactions in a Diesel Oxidation Catalyst. *Environ. Sci. Technol.* **2014**, *48*, 2361–2367. [CrossRef] [PubMed]
21. Pan, Y.; Xu, L.; Huang, L.; He, W.; Li, H.; Wang, S.; Long, Z.; Sun, Z. Identification of active sites in Pt–Co bimetallic catalysts for CO oxidation. *ACS Appl. Energy Mater.* **2021**, *4*, 11151–11161. [CrossRef]
22. Du, Y.; Zou, J.; Guo, Y.; Xu, X.; Chen, H.; Su, C.; Zeng, Z.; Li, L. A novel viewpoint on the surface adsorbed oxygen and the atom doping in the catalytic oxidation of toluene over low-Pt bimetal catalysts. *Appl. Catal. A Gen.* **2021**, *609*, 117913. [CrossRef]
23. Acar, C.; Dincer, I. The potential role of hydrogen as a sustainable transportation fuel to combat global warming. *Int. J. Hydrogen Energy* **2020**, *45*, 3396–3406. [CrossRef]
24. Shadidi, B.; Najafi, G.; Yusaf, T. A review of hydrogen as a fuel in internal combustion engines. *Energies* **2021**, *14*, 6209. [CrossRef]
25. Hernández, J.J.; Cova-Bonillo, A.; Wu, H.; Barba, J.; Rodríguez-Fernández, J. Low temperature autoignition of diesel fuel under dual operation with hydrogen and hydrogen-carriers. *Energy Convers. Manag.* **2022**, *258*, 115516. [CrossRef]

26. Nag, S.; Sharma, P.; Gupta, A.; Dhar, A. Experimental study of engine performance and emissions for hydrogen diesel dual fuel engine with exhaust gas recirculation. *Int. J. Hydrogen Energy* **2019**, *44*, 12163–12175. [CrossRef]
27. Mhadeshwar, A.B.; Vlachos, D.G. Microkinetic modeling for water-promoted CO oxidation, water-gas shift, and preferential oxidation of CO on Pt. *J. Phys. Chem. B* **2004**, *108*, 15246–15258. [CrossRef]
28. Piqueras, P.; de la Morena, J.; Sanchis, E.J.; Conde, C.; Herreros, J.M.; Tsolakis, A. Potential of H2-Assisted Light-Off of Oxidation Catalyst in H2-Diesel Dual-Fuel Engines. In Proceedings of the Internal Combustion Engine Division Fall Technical Conference. American Society of Mechanical Engineers, Pittsburgh, PA, USA, 8–11 October 2023; Volume 87561, p. V001T05A001. [CrossRef]
29. Piqueras, P.; Pla, B.; Sanchis, E.J.; García, E. Control-Oriented Reduced-Order Modelling of Conversion Efficiency in Dual-Layer Washcoat Catalysts with Accumulation and Oxidation Functions. In Proceedings of the Internal Combustion Engine Division Fall Technical Conference, Indianapolis, IN, USA, 16–19 October 2022; American Society of Mechanical Engineers: New York, NY, USA, 2022; Volume 86540, p. V001T04A001. [CrossRef]
30. Desantes, J.M.; Galindo, J.; Payri, F.J.; Piqueras, P.; Serrano, J.R. Device for Atmosphere Conditioning for Testing Combustion Engines, and Associated Method and Use. Patent WO 2015/110683 A1, 30 July 2015.
31. Desantes, J.M.; Galindo, J.; Payri, F.J.; Piqueras, P.; Serrano, J.R. Device for Conditioning the Atmosphere in Test of Alternative Internal Combustion Engines, Method and Use of Said Device. Patent WO 2016/116642 A1, 28 July 2016.
32. Herreros, J.M.; Gill, S.S.; Lefort, I.; Tsolakis, A.; Millington, P.; Moss, E. Enhancing the low temperature oxidation performance over a Pt and a Pt-Pd diesel oxidation catalyst. *Appl. Catal. B Environ.* **2014**, *147*, 835–841. [CrossRef]
33. Martin, J.; Arnau, F.; Piqueras, P.; Auñon, A. *Development of an Integrated Virtual Engine Model to Simulate New Standard Testing Cycles*; Technical report, Paper 2018-01-1413; SAE: Warrendale, PA, USA, 2018. [CrossRef]
34. Piqueras, P.; Ruiz, M.J.; Herreros, J.M.; Tsolakis, A. Sensitivity of pollutants abatement in oxidation catalysts to the use of alternative fuels. *Fuel* **2021**, *297*, 120686. [CrossRef]
35. Piqueras, P.; Ruiz, M.J.; Herreros, J.M.; Tsolakis, A. Influence of the cell geometry on the conversion efficiency of oxidation catalysts under real driving conditions. *Energy Convers. Manag.* **2021**, *233*, 113888. [CrossRef]
36. Kryl, D.; Kočí, P.; Kubíček, M.; Marek, M.; Maunula, T.; Härkönen, M. Catalytic converters for automobile diesel engines with adsorption of hydrocarbons on zeolites. *Ind. Eng. Chem. Res.* **2005**, *44*, 9524–9534. [CrossRef]
37. Bissett, E.J. An Asymptotic Solution for Washcoat Pore Diffusion in Catalytic Monoliths. *Emiss. Control. Sci. Technol.* **2015**, *1*, 3–16. [CrossRef]
38. Ratnakar, R.R.; Dadi, R.K.; Balakotaiah, V. Multi-scale reduced order models for transient simulation of multi-layered monolith reactors. *Chem. Eng. J.* **2018**, *352*, 293–305. [CrossRef]
39. Sharma, H.; Mhadeshwar, A. A detailed microkinetic model for diesel engine emissions oxidation on platinum based diesel oxidation catalysts (DOC). *Appl. Catal. B Environ.* **2012**, *127*, 190–204. [CrossRef]
40. Gieshoff, J.; Schäfer-Sindlinger, A.; Spurk, P.; Van Den Tillaart, J.; Garr, G. *Improved SCR Systems for Heavy Duty Applications*; Technical report, Paper 2000-01-0189; SAE: Warrendale, PA, USA, 2000. [CrossRef]
41. Rhodes, C.; Hutchings, G.; Ward, A. Water-gas shift reaction: Finding the mechanistic boundary. *Catal. Today* **1995**, *23*, 43–58. [CrossRef]
42. Lagarias, J.C.; Reeds, J.A.; Wright, M.H.; Wright, P.E. Convergence Properties of the Nelder–Mead Simplex Method in Low Dimensions. *SIAM J. Optim.* **1998**, *9*, 112–147. [CrossRef]